

# **Searches for invisibly decaying Higgs bosons with the CMS detector**

Patrick James Dunne  
of Imperial College London

A dissertation submitted to Imperial College London  
for the degree of Doctor of Philosophy

## Abstract

## Declaration

This dissertation is the result of my own work, except where explicit reference is made to the work of others, and has not been submitted for another qualification to this or any other university. This dissertation does not exceed the word limit for the respective Degree Committee.

Patrick Dunne

## Acknowledgements

# Contents

<b>1</b>	<b>Introduction and theory</b>	<b>2</b>
1.1	The standard model of particle physics . . . . .	2
1.1.1	Fundamental particles in nature . . . . .	3
1.1.2	Introduction to gauge theories . . . . .	4
1.2	The SM gauge group and fundamental particle representations . . . . .	6
1.2.1	Spontaneous symmetry breaking and the Higgs mechanism . . . . .	8
1.2.2	Higgs boson production and decay at the LHC . . . . .	9
1.2.3	Challenges for the SM . . . . .	9
1.3	Dark matter . . . . .	9
1.4	Some extensions of the standard model incorporating dark matter . . . . .	9
<b>2</b>	<b>The LHC and the CMS experiment</b>	<b>10</b>
2.1	The LHC . . . . .	10
2.2	The CMS experiment . . . . .	16
2.2.1	Tracker . . . . .	18
2.2.2	Electromagnetic calorimeter . . . . .	19
2.2.3	Hadronic calorimeter . . . . .	21
2.2.4	Muon system . . . . .	22
2.2.5	Trigger system and data processing . . . . .	25
<b>3</b>	<b>Physics objects and event reconstruction</b>	<b>28</b>
3.1	Primary vertex . . . . .	28
3.2	Jets . . . . .	28
3.3	Missing transverse energy . . . . .	28
3.4	Electrons . . . . .	28
3.5	Muons . . . . .	28
3.6	Taus . . . . .	28
3.7	Photons . . . . .	28

<b>4 Methods for limit setting</b>	<b>29</b>
<b>5 Search for invisibly decaying Higgs bosons in run I prompt data</b>	<b>30</b>
5.1 Trigger and event selection . . . . .	30
5.2 Background estimation . . . . .	30
5.2.1 $W \rightarrow e\nu + \text{jets}$ . . . . .	30
5.2.2 $W \rightarrow \mu\nu + \text{jets}$ . . . . .	30
5.2.3 $W \rightarrow \tau\nu + \text{jets}$ . . . . .	30
5.2.4 $Z \rightarrow \nu\nu + \text{jets}$ . . . . .	30
5.2.5 QCD . . . . .	30
5.2.6 Minor backgrounds . . . . .	30
5.3 Systematic uncertainties . . . . .	30
5.4 Results . . . . .	30
<b>6 Search for invisibly decaying Higgs bosons in run I parked data</b>	<b>31</b>
6.1 Trigger . . . . .	32
6.2 Event selection . . . . .	32
6.3 Background estimation . . . . .	32
6.3.1 $W \rightarrow e\nu + \text{jets}$ . . . . .	32
6.3.2 $W \rightarrow \mu\nu + \text{jets}$ . . . . .	32
6.3.3 $W \rightarrow \tau\nu + \text{jets}$ . . . . .	32
6.3.4 $Z \rightarrow \nu\nu + \text{jets}$ . . . . .	32
6.3.5 QCD . . . . .	32
6.3.6 Minor backgrounds . . . . .	32
6.4 Systematic uncertainties . . . . .	32
6.5 Results . . . . .	32
<b>7 Combinations and interpretations of run I searches for invisibly decaying Higgs bosons</b>	<b>33</b>
7.1 Searches in other channels . . . . .	33
7.2 Combination with prompt VBF search . . . . .	33
7.3 Combination with the parked VBF search . . . . .	33
7.4 Dark matter interpretations . . . . .	33
<b>8 Search for invisibly decaying Higgs bosons in run II data</b>	<b>34</b>
<b>Bibliography</b>	<b>36</b>

<b>List of Figures</b>	<b>38</b>
<b>List of Tables</b>	<b>39</b>
<b>Acronyms</b>	<b>40</b>

# Chapter 1

## Introduction and theory

This chapter will explain the theory of invisible decays of the Higgs boson (“Higgs to invisible”). It will start with an introduction to the standard model (SM), focussing on the Higgs mechanism, before outlining the motivations behind and some candidates for physics beyond the SM (BSM). Natural units, where  $\hbar = c = 1$ , Einstein summation convention and Feynman slash notation are used throughout. Four vector indices are labelled using greek letters, and gauge group generators using roman letters.

### 1.1 The standard model of particle physics

The SM describes the interaction of the particles currently thought to be fundamental with the strong, weak and electromagnetic forces. Its predictions, which come from specifying the symmetries the theory respects and how they are broken, the particles in the theory, and 18 free parameters, have been tested in many different experiments, in some cases up to one part in a trillion [1]. However, it does face challenges, described in section Section 1.2.3, one example being that it does not describe dark matter.

The SM is a gauge invariant quantum field theory (QFT). To construct a QFT the symmetries that are respected by the theory and the fields it describes must be specified. The symmetries are important because of Noether’s theorem, which states that for every continuously differentiable symmetry of the Lagrangian of a theory there is a corresponding conservation law [2,3]. An example of this is Poincaré invariance, the invariance of the laws of physics under translations and rotations in space and time, which leads through Noether’s theorem to the conservation of energy, linear momentum and angular momentum. In addition to giving rise to conservation laws, some types of

**Table 1.1:** The fundamental fermions observed in nature separated into their three generations. Each particle shown also has an antiparticle with opposite charge and identical mass. Values taken from [5]

Generation	Leptons			Hadrons		
	Particle	Mass	Charge	Particle	Mass	Charge
1	$e^-$	511 keV	-1	u	2.3 MeV	$+\frac{2}{3}$
	$\nu_e$	$\sim 0$	0	d	4.8 MeV	$-\frac{1}{3}$
2	$\mu^-$	105.7 MeV	-1	c	1.275 GeV	$+\frac{2}{3}$
	$\nu_\mu$	$\sim 0$	0	s	95 MeV	$-\frac{1}{3}$
3	$\tau^-$	1.777 GeV	-1	t	173.2 GeV	$+\frac{2}{3}$
	$\nu_\tau$	$\sim 0$	0	b	4.18 GeV	$-\frac{1}{3}$

symmetry lead to additional fields being required to preserve invariance, this will be discussed further in Section 1.1.2 [4].

It is important to specify the fields described by the QFT as these are constrained by the fundamental particles seen in nature. This is because particles correspond to the quantised excitations of fields. Specifically, scalar fields correspond to spin zero bosons, spinor fields correspond to spin half fermions, and vector fields correspond to spin 1 bosons. In order to add a new field an explanation for why the corresponding particle has not yet been observed must, therefore, be provided. We will now go through the particles observed in nature and how they are represented in the SM.

### 1.1.1 Fundamental particles in nature

There are two types of fundamental particles in nature, fermions and bosons. The fermions observed in nature that are currently thought to be fundamental are then divided into those which interact via the strong nuclear force (the quarks), and those which don't (the leptons). Both the quarks and leptons have two further types: charged and neutral in the case of the leptons, and up type and down type in the case of the fermions. Another interesting feature of the fermions is that they are arranged in three generations. Each generation has one fermion of each type with the same quantum numbers as those in the other generations, except that the mass is different. Table 1.1 shows this structure.

**Table 1.2:** The fundamental vector bosons observed in nature separated by the force which they mediate. Values taken from [5].

Force	Particle	Mass	Charge
Electromagnetism	$\gamma$	0	0
Weak	$W^\pm$	80.4 GeV	$\pm 1$
	Z	91.2 GeV	0
Strong	g	0	0

The bosons in nature also have two types. The first type are vector bosons which mediate the three fundamental interactions described by the SM. The vector bosons are summarised in Table 1.2, where it can be seen that their masses are very different, the photon and the eight gluons being massless, while the  $W^\pm$  and Z bosons are very massive. As we will see in Section 1.2.1 explaining these masses requires the Higgs mechanism. The Higgs mechanism also gives rise to the other type of boson seen in nature, the scalar Higgs boson. In order to see how all of the above particles are represented in the SM an introduction to gauge theories is necessary.

### 1.1.2 Introduction to gauge theories

Gauge symmetries are local transformations, i.e. the transformation can be different at different points in space and time, that form a symmetry group. To see the effect of imposing such a symmetry on a theory consider imposing local invariance under U(1) transformations on the Dirac Lagrangian for a massive fermion:

$$\mathcal{L} = i\bar{\psi}\not{\partial}\psi - m\bar{\psi}\psi \quad [6]. \quad (1.1)$$

This Lagrangian is invariant under a global  $U(1)$  transformation  $\psi \rightarrow e^{iq\theta}\psi$ , where q and  $\theta$  are constant. However, if the  $U(1)$  transformation is local i.e.  $\theta$  is a function of spacetime position the Lagrangian is no longer invariant and transforms as:

$$\mathcal{L} \rightarrow \mathcal{L} - q(\partial_\mu\theta)\bar{\psi}\gamma^\mu\psi. \quad (1.2)$$

In order to restore invariance a vector field,  $A_\mu$ , referred to as a gauge field or gauge boson, which transforms as  $A_\mu \rightarrow A_\mu + \partial_\mu \theta$  and has an interaction with the fermion field:

$$\mathcal{L}_{int} = q(\bar{\psi}\gamma^\mu\psi)A_\mu, \quad (1.3)$$

can be added to the theory. The interaction term of the new gauge field transforms as:

$$\mathcal{L}_{int} \rightarrow \mathcal{L}_{int} + q(\partial_\mu\theta)\bar{\psi}\gamma^\mu\psi, \quad (1.4)$$

which cancels out the non-gauge invariance seen in equation (1.2).

Assuming the new gauge field to be massless the Lagrangian is now:

$$\mathcal{L} = i\bar{\psi}\not{\partial}\psi - m\bar{\psi}\psi + q(\bar{\psi}\gamma^\mu\psi)A_\mu - \frac{1}{4}F_{\mu\nu}F^{\mu\nu}, \quad (1.5)$$

where  $F_{\mu\nu}$  is the field strength tensor of the vector field. For a gauge boson from a general gauge group is written as:

$$F_{\mu\nu}^a = \partial_\mu A_\nu^a - \partial_\nu A_\mu^a + g f^{abc} A_\mu^b A_\nu^c, \quad (1.6)$$

where  $f^{abc}$  are the structure constants of the gauge group, which are a representation of the comutation relations between the group's generators. For  $U(1)$  which only has one self-commuting generator the single structure constant is 0. However, for non-Abelian gauge groups (i.e. those with non-commuting generators) they can be non-zero causing the  $F_{\mu\nu}F^{\mu\nu}$  term in the Lagrangian to include self-interaction terms of the vector bosons.

It is also interesting to note that equation (1.5) can be rewritten as:

$$\mathcal{L} = i\bar{\psi}\gamma^\mu\mathcal{D}_\mu\psi - m\bar{\psi}\psi - \frac{1}{4}F_{\mu\nu}F^{\mu\nu}, \quad (1.7)$$

where  $\mathcal{D}_\mu = \partial_\mu + iqA_\mu$  and is referred to as the covariant derivative. Comparing equation (1.1) and equation (1.7) it can be seen that to go from a globally invariant Lagrangian to a locally invariant one we have substituted the normal spacetime derivative for the covariant derivative and added the free term of the vector field.

$U(1)$  transformations have one degree of freedom and can be described by one parameter, in the above case  $\theta$ , and in order to make the Lagrangian locally invariant one interacting gauge boson had to be added. This correspondence between the number of degrees of freedom and the number of gauge bosons holds generally. For each degree of freedom of

a group's transformations there exists a generator of the group, and for each generator one interacting gauge boson must be added to achieve local invariance.

## 1.2 The SM gauge group and fundamental particle representations

The SM is gauge invariant under the group  $SU(3)_C \otimes SU(2)_L \otimes U(1)_Y$ . Fermions in the SM are spin half spinor representations of these symmetry groups. These spinors can be split into chirally left and right handed components using the projection operators  $P_L = \frac{1}{2}(1 \mp \gamma^5)$ . Chirally left and right handed fermions transform differently under  $SU(2)_L$ . The right handed spinors are not charged under  $SU(2)_L$  and thus are represented as a singlet, while the left handed spinors transform as a doublet.

The first generation of leptons can, therefore, be written as:

$$\psi_1 = e_R, \psi_2 = L = \begin{pmatrix} \nu_e \\ e_L \end{pmatrix}. \quad (1.8)$$

The SM treats neutrinos as massless and has no right handed neutrino. Similarly the first generation of quarks can be written as:

$$\psi_3 = u_R, \psi_4 = d_R, \psi_5 = \begin{pmatrix} u_L \\ d_L \end{pmatrix}. \quad (1.9)$$

As we saw in Section 1.1.2 gauge symmetries in theories with fermions require the addition of an interacting vector boson per symmetry generator to preserve gauge invariance.  $SU(3)_C$  has eight generators whose eight vector bosons,  $G_{a\mu}$ , correspond to the eight physical gluons which mediate the strong interaction.  $SU(2)_L$  has three generators whose three vector bosons,  $W_\mu^i$ , mix with the one vector boson from  $U(1)_Y$ ,  $B_\mu$  unifying the electromagnetic and weak forces into one electroweak force. The physical states that

result are:

$$\begin{aligned} W^\pm_\mu &= \frac{1}{\sqrt{2}} (W^1_\mu \mp i W^2_\mu) \\ Z_\mu &= \cos(\theta_W) W^3_\mu - \sin(\theta_W) B_\mu \\ A_\mu &= \sin(\theta_W) W^3_\mu + \cos(\theta_W) B_\mu, \end{aligned} \tag{1.10}$$

where  $\theta_W$  is the Weinberg angle and  $A_\mu$  is the photon field. Also, as described in Section 1.1.2 the interaction between these vector bosons and the fermion fields occurs through their presence in the covariant derivative, and interactions between the vector bosons occur because  $SU(3)_C$  and  $SU(2)_L$  are non-Abelian.

Now let us try to construct a Lagrangian for these fields. First ignoring the masses we find:

$$\mathcal{L} = i\bar{\psi}_i \not{\mathcal{D}} \psi_i - \frac{1}{4} F_{\mu\nu j} F_j^{\mu\nu}, \tag{1.11}$$

where the sum over all  $\psi$  also includes the second and third generations,  $F_{\mu\nu j} F_j^{\mu\nu}$  is a sum of the free terms of all the SM gauge bosons and  $\not{\mathcal{D}}$  is the SM covariant derivative:

$$\mathcal{D}_\mu = \partial_\mu + ig_1 \frac{Y}{2} B_\mu + ig_2 \frac{\tau_i}{2} W_\mu^i + ig_3 \frac{\lambda_a}{2} G_\mu^a, \tag{1.12}$$

with  $Y$  being the constant generator of  $U(1)$ ,  $\tau_i$  the generators of  $SU(2)_L$ ,  $\lambda_a$  the generators of  $SU(3)_C$  and  $g_i$  the coupling constants of the fields. It should be noted that  $\frac{g_1}{g_2}$  is equal to  $\tan(\theta_W)$ .

When we try to include mass a problem occurs. We know that some of the fermions have mass, and consequently we should have fermion mass terms of the form:

$$\begin{aligned} \mathcal{L}_{m_f} &= -m_f \bar{f} f \\ &= -m_f \bar{f} \left[ \frac{1}{2} (1 - \gamma^5) + \frac{1}{2} (1 + \gamma^5) \right] f \\ &= -m_f (\bar{f}_R f_L + \bar{f}_L f_R), \end{aligned} \tag{1.13}$$

in our Lagrangian. However, as the left and right handed fields do not transform in the same way under  $SU(2)_L$  this term breaks the gauge symmetry of the Lagrangian and can't be present.

A similar problem occurs for vector fields. In Section 1.1.2 we didn't consider the mass term of these vector fields:

$$\mathcal{L}_{m_V} = \frac{1}{2} m_V^2 A_\mu A^\mu, \quad (1.14)$$

which is not gauge invariant, so massive vector bosons are not possible on their own in gauge invariant theories either. The additional piece of the SM required to allow particles to have mass is the Higgs mechanism.

### 1.2.1 Spontaneous symmetry breaking and the Higgs mechanism

The Higgs mechanism is a form of spontaneous symmetry breaking. A symmetry is said to be spontaneously broken when the Lagrangian remains invariant while the vacuum state, i.e. that with lowest energy, does not. Terms which are not gauge invariant can then be incorporated into the theory by adding a field which has a non-zero vacuum expectation value and coupling it to the other fields present in the term. For the Higgs mechanism this field is a complex scalar  $SU(2)_L$  doublet, called the Higgs field:

$$\phi = \begin{pmatrix} \phi^+ \\ \phi^0 \end{pmatrix}. \quad (1.15)$$

The main part of the Higgs field Lagrangian is:

$$\mathcal{L} = T - V = (\mathcal{D}_\mu \phi)^\dagger (\mathcal{D}^\mu \phi) + \mu^2 \phi^\dagger \phi - \lambda (\phi^\dagger \phi)^2. \quad (1.16)$$

For  $\mu^2 > 0$  the minima of the potential are non-zero and form a circle in phase space of  $\phi$ . All of these vacua are equivalent and a particular vacuum can be chosen with no physical effect. By convention we choose the following vacuum:

$$\langle 0 | \phi | 0 \rangle = \begin{pmatrix} 0 \\ \sqrt{\frac{\mu^2}{2\lambda}} \end{pmatrix} = \frac{1}{\sqrt{2}} \begin{pmatrix} 0 \\ v \end{pmatrix}. \quad (1.17)$$

Next we consider small perturbations around this vacuum, ignoring those that can be set to zero by gauge freedom gives:

$$\phi = \begin{pmatrix} 0 \\ v + H \end{pmatrix}. \quad (1.18)$$

Inserting this into equation (1.16) and ignoring terms with more than one type of field gives at leading order:

$$\mathcal{L} = \frac{1}{2}\partial_\mu H\partial^\mu H - \frac{1}{2}\mu^2 H^2 + \frac{v^2}{8} [g_2^2 W_\mu^+ W^{+\mu} + g_2^2 W_\mu^- W^{-\mu} + (g_1^2 + g_2^2) Z_\mu Z^\mu]. \quad (1.19)$$

As expected, the weak vector bosons  $W_\mu^\pm$  and  $Z_\mu$  acquire masses  $\frac{gv}{2}$  and  $\frac{v}{2}\sqrt{g_1^2 + g_2^2}$  respectively. We also see an additional massive scalar  $H$ , which is the Higgs boson, which has mass  $\sqrt{2}\mu$ . The photon and gluons do not acquire masses as the particular choice of coupling constants and the structure of the group generators leads to the terms in  $A_\mu$  and  $G_{\mu a}$  being zero.

The final part of the Higgs field Lagrangian is that giving rise to the fermion masses. These are generated by a Yukawa term in the Lagrangian for each fermion as follows:

$$\mathcal{L}_{Yuk} = k_f (\bar{f}_L \phi f_R + \bar{f}_R \phi^\dagger f_L). \quad (1.20)$$

The fermion's mass is then  $\frac{k_f v}{\sqrt{2}}$ .

### 1.2.2 Higgs boson production and decay at the LHC

### 1.2.3 Challenges for the SM

## 1.3 Dark matter

## 1.4 Some extensions of the standard model incorporating dark matter

# Chapter 2

## The LHC and the CMS experiment

The purpose of this chapter is to introduce the CMS experiment [7] and the LHC [8]. Without both of these apparatus the analyses performed for this thesis would, of course, not have been possible. In Section 2.1 an overview of the LHC and the chain of accelerators which feed into it will be given. This will then be followed in Section 2.2 by a description of the CMS experiment focussing on the aspects most relevant to the search for invisibly decaying Higgs bosons.

### 2.1 The LHC

The LHC is situated 100m underground in a tunnel formerly built for the LEP accelerator [9] at CERN near Geneva, Switzerland. It is a 27km storage ring which accelerates both protons and heavy ions and collides them at the highest centre of mass energies of any collider built to date. The work contained in this thesis uses data from proton-proton collisions (“events”). These protons are obtained by taking hydrogen gas and stripping its atoms of their electrons with an electric field. The first accelerator in the LHC accelerator sequence, Linac 2, accelerates the protons to 50 MeV. The protons are then accelerated to 1.4 GeV by the next accelerator, the Proton Synchrotron Booster (PSB), which is followed by the Proton Synchrotron (PS) where they reach 25 GeV. The beam energy is then increased to 450 GeV in the Super Proton Synchrotron (SPS). Finally, the protons are injected into the LHC where, at time of writing, the maximum energy the beams have been accelerated to is 6.5 TeV, close to the design maximum of 7 TeV.

When fully filled the LHC contains two counter-rotating beams which are formed of up to 2808 bunches spaced either 25 or 50 ns apart and each containing  $\mathcal{O}(10^{11})$  protons.

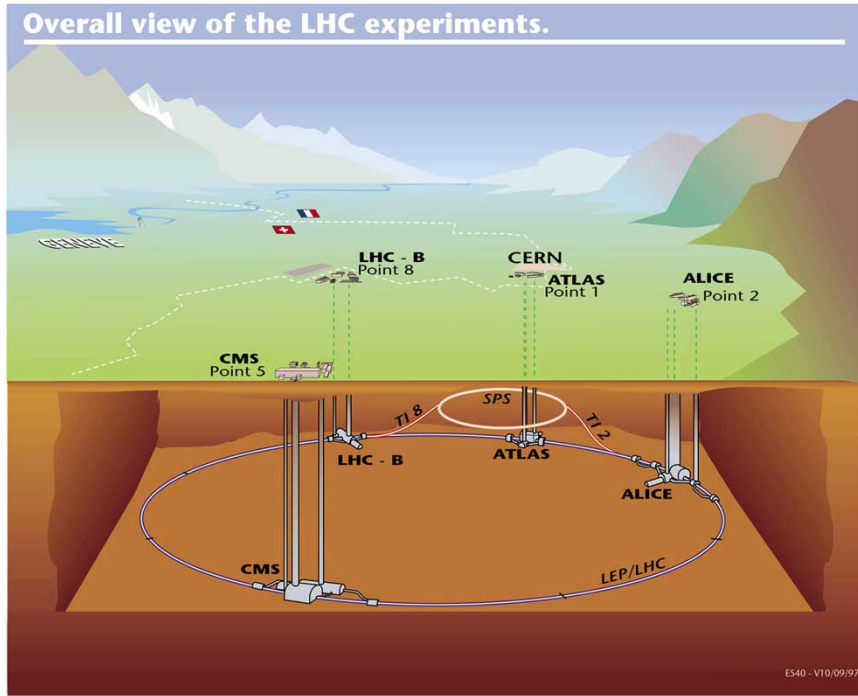


**Figure 2.1:** The layout of the LHC accelerator chain, showing the position of the four main detectors.

The two beams are kept travelling in a circle by 1232 superconducting dipole magnets and steered to four collision points around the LHC. Detectors are situated at these collision points to observe the collisions, the main four being: ALICE [10], ATLAS [11], CMS [7] and LHCb [12]. A schematic of the LHC accelerator chain and the detectors can be seen in Figure 2.1.

When studying a physical process occurring in particle collisions it is important to know how many times it will occur, this can be expressed as:

$$N = \mathcal{L}\sigma, \quad (2.1)$$

where  $\mathcal{L}$ , the integrated luminosity, depends only on the parameters of the collisions, and the cross-section depends only on the process. In order to observe rare (i.e. low cross-section) processes, such as those studied at the LHC, it is, necessary to use very high luminosity datasets. The integrated luminosity is obtained by integrating the instantaneous luminosity over time, so large luminosities can be obtained either by running the accelerator for a long time, or by operating at high instantaneous luminosity.

For collisions at the LHC the instantaneous luminosity is given by:

$$\mathcal{L} = \frac{k_b N_b^2 f_{rev} \gamma}{4\pi \epsilon_n \beta} [13], \quad (2.2)$$

where  $k_b$  is the number of bunches per beam,  $N_b$  the number of protons per bunch,  $f_{rev}$  the revolution frequency,  $\epsilon_n$  the normalised transverse beam emittance,  $\beta^*$  the beta-function at the interaction point and  $\gamma$  the Lorentz factor. The design instantaneous luminosity of the LHC is  $10^{34} \text{ cm}^{-2}\text{s}^{-1}$  with 25ns bunch spacing.

The LHC started physics runs in 2010, during which it operated at a centre of mass energy of 7 TeV and delivered an integrated luminosity of  $44.2 \text{ pb}^{-1}$  to CMS. In 2011 the LHC also operated at 7 TeV and delivered  $6.1 \text{ fb}^{-1}$  to CMS. The centre of mass energy was increased to 8 TeV in 2012 and  $23.3 \text{ fb}^{-1}$  of data were delivered to CMS. A summary of the luminosity delivered to CMS during the three periods of run 1 can be seen in Figure 2.2. In run 2 the centre of mass energy was further increased to 13 TeV and during 2015  $4.09 \text{ fb}^{-1}$  of data were delivered to CMS at this energy. In order to be used for physics analysis data must be certified. This certification ensures that the detector was fully operational when the data were recorded. In 2011  $5.1 \text{ fb}^{-1}$  were certified, in 2012  $19.7 \text{ fb}^{-1}$  were certified and in 2015  $2.2 \text{ fb}^{-1}$  were certified.

The cross-section for several processes is shown in Figure 2.3 and it can be seen that the cross-section for VBF Higgs production is approximately  $1.5 \text{ pb}$ . Therefore, we expect approximately 30000 VBF produced Higgs bosons in the 2012 dataset. By contrast the vector boson production cross section is approximately  $100 \text{ nb}$  and the total cross-section for any process is orders of magnitude higher still. The separation of the relatively small number of signal events from the large background is a major challenge for the search for Higgs to invisible.

The large total cross-section combined with the high instantaneous luminosities that the LHC operates at leads to the probability for multiple proton-proton interactions per bunch crossing being high. The distribution of the number of interactions per bunch crossing can be seen in Figure 2.4. The additional interactions on top of the process of interest in a bunch crossing are called pile-up pile-up (PU).

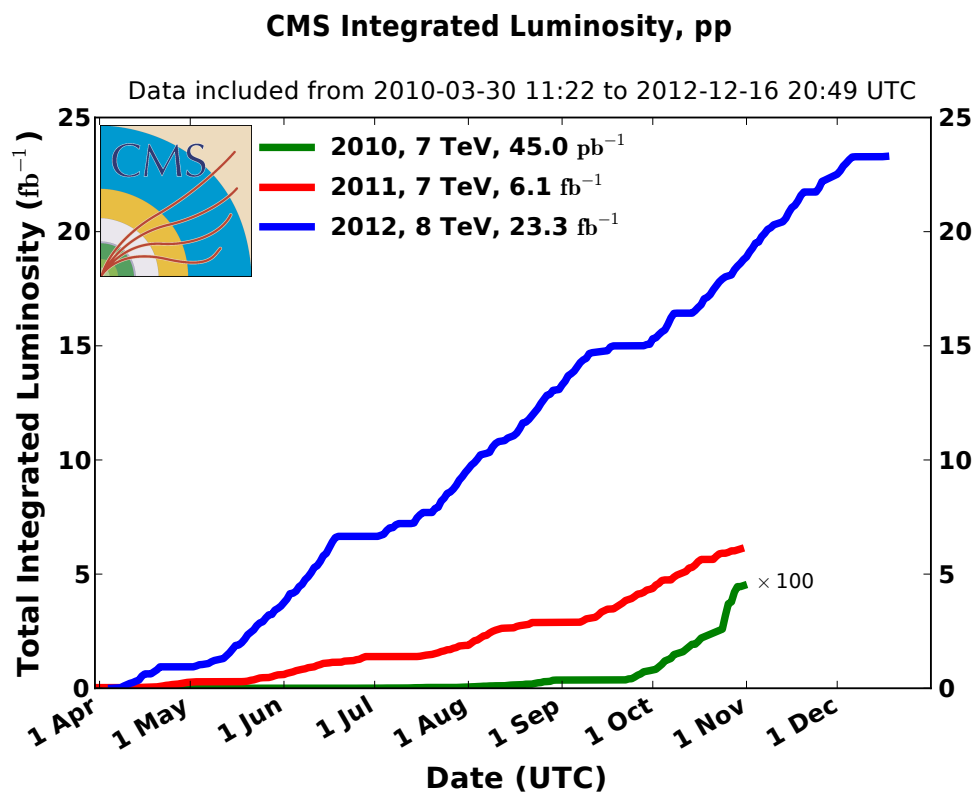
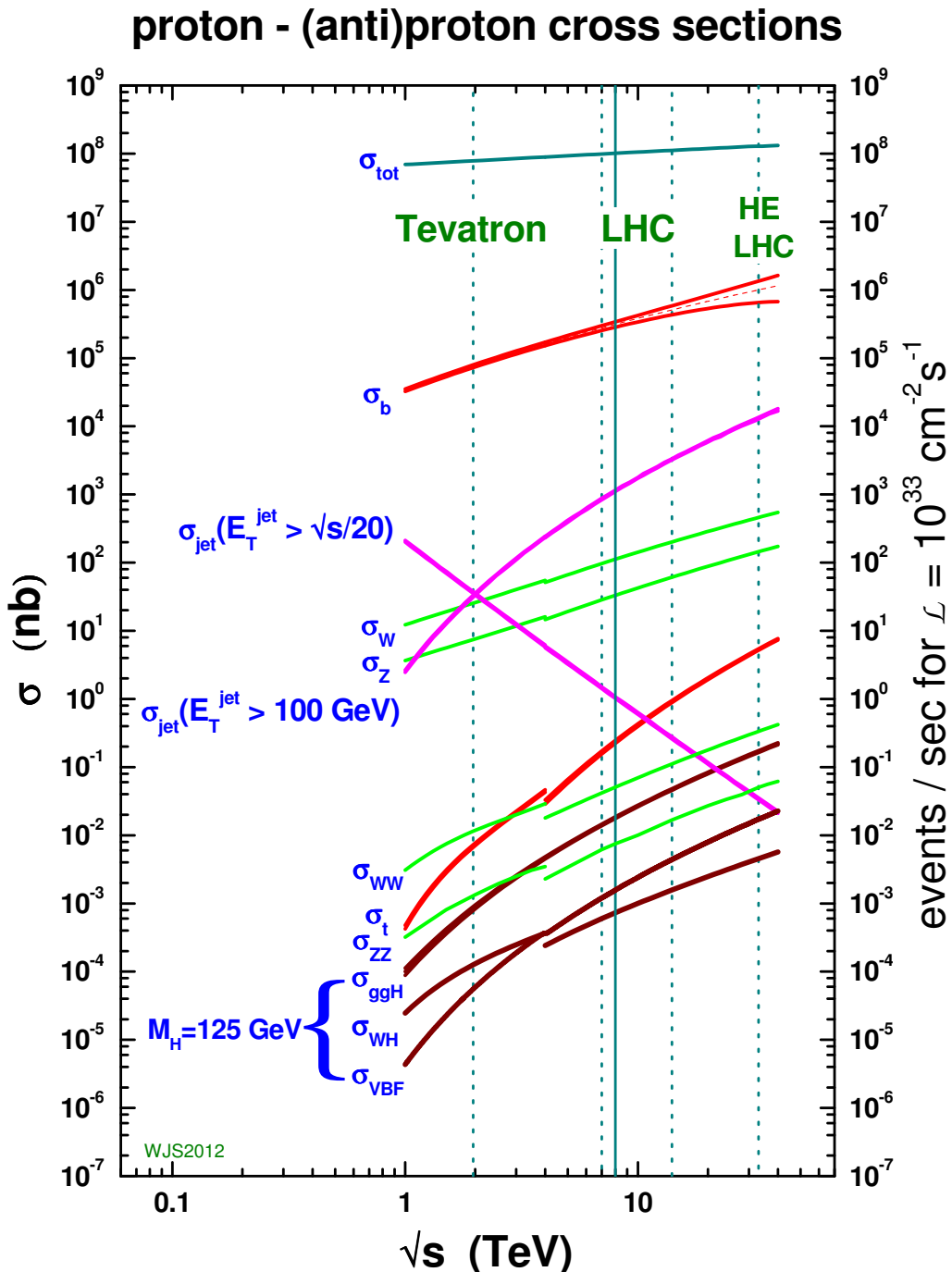
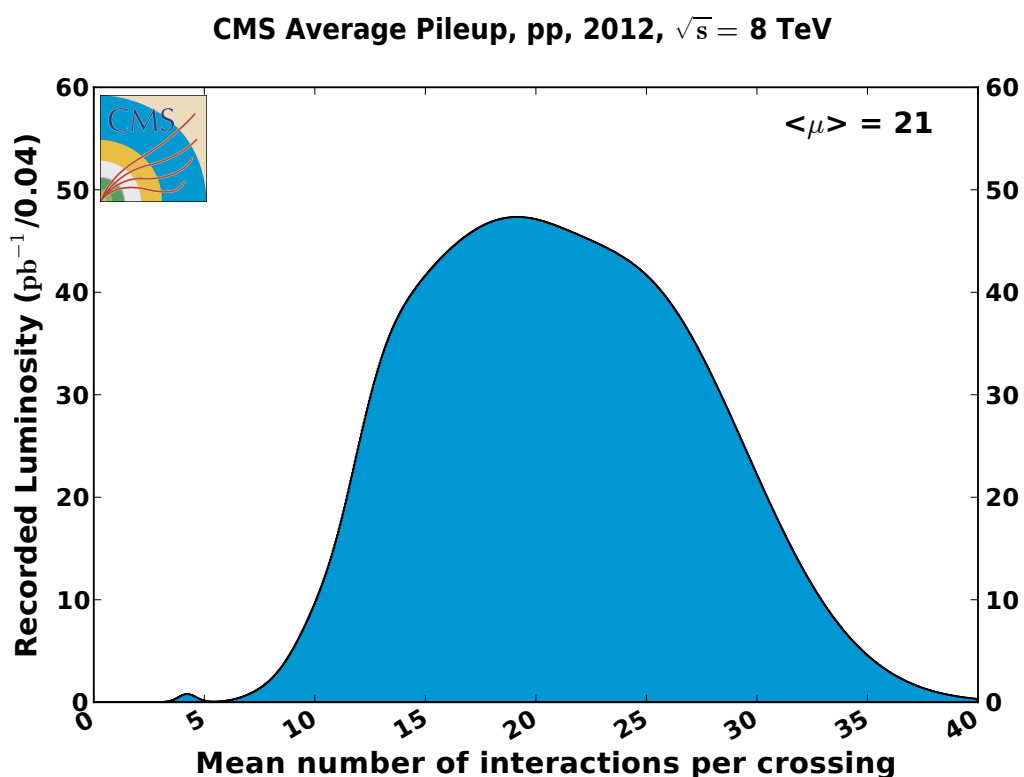


Figure 2.2: A summary of the luminosity delivered to CMS during Run 1 of the LHC [14].



**Figure 2.3:** Cross sections for several processes in collisions of protons with protons or anti-protons as a function of centre of mass energy. The energies that the LHC and Tevatron ran at are highlighted [15].



**Figure 2.4:** Distribution of the number of interactions per bunch crossing in CMS during 2012 running of the LHC [14].

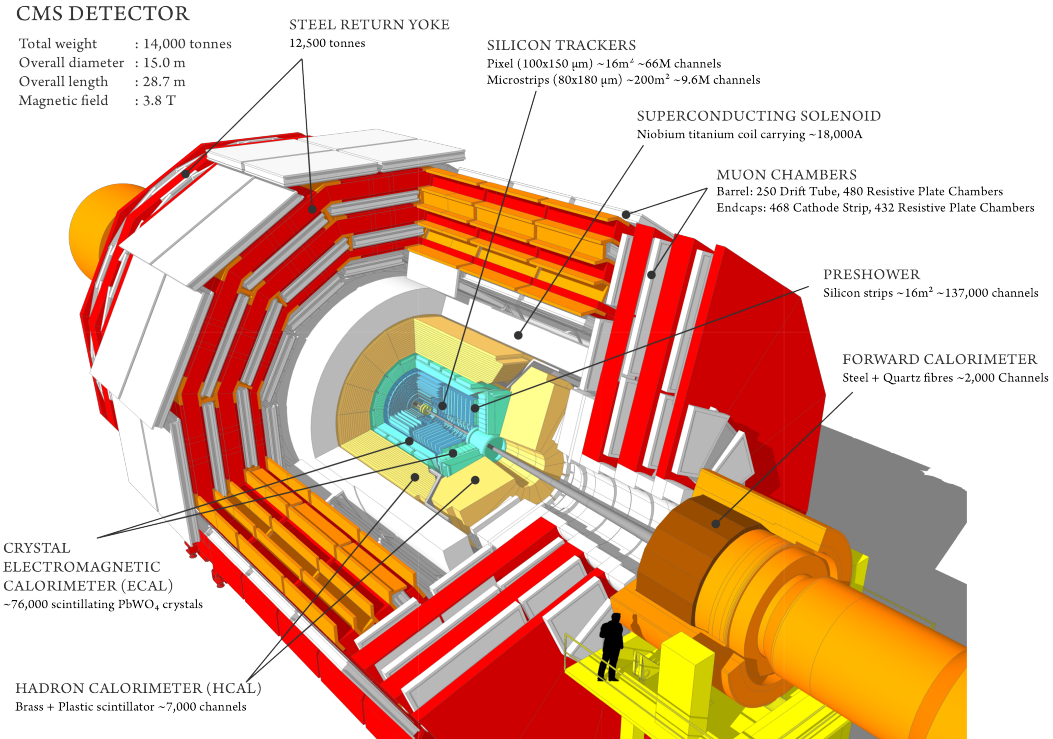


**Figure 2.5:** A diagram of the subsystems making up the CMS detector, illustrating the hermeticity and layered structure of the experiment [16].

## 2.2 The CMS experiment

The CMS detector was designed to search for the SM Higgs and new physics at the TeV energy scale. Both because the nature of new physics is not known and the SM Higgs has a wide range of decays and production mechanisms CMS must be sensitive to many different types of final state particles and topologies. In order to achieve this it has a hermetic design comprising a barrel, endcaps and a forward calorimetry system, and is also composed of several layers of subdetectors each sensitive to different particles as shown in Figure 2.5. The hermeticity of the detector is particularly important for the VBF Higgs to invisible search, because, as described in Section 1.2.2, the VBF final state is highly likely to have jets in the forward regions of the detector.

A central design feature of CMS is the superconducting magnet, inside which is generated a 3.8T axial field. This field bends the path of charged particles travelling through it allowing their momentum to be measured. Not all particles are charged however, and the path of several types of particles through the CMS detector is shown in Figure 2.6. The first layer is the tracker which records the paths taken by charged particles, as well as providing a momentum measurement the tracks also allow the vertex the particle came

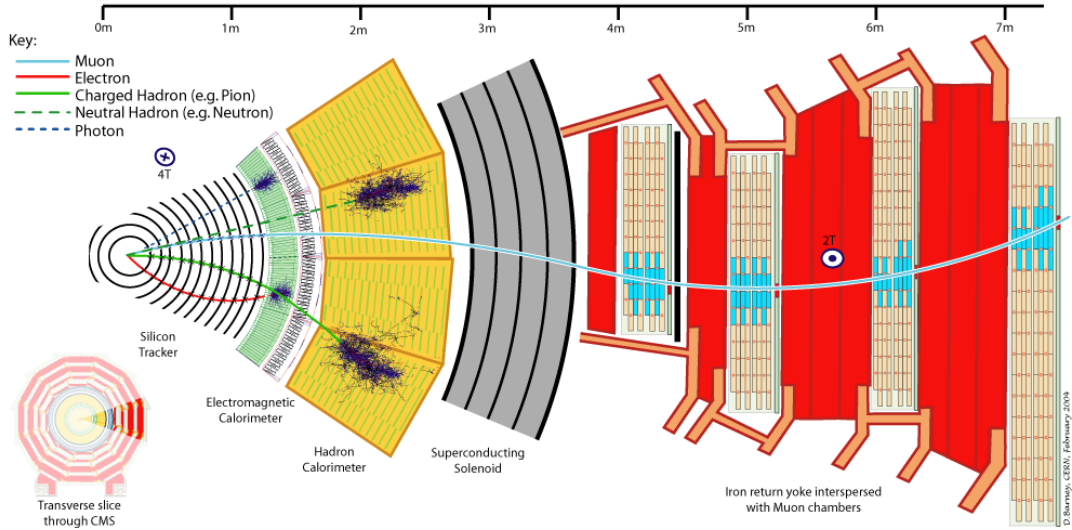


**Figure 2.6:** A schematic cross-section of the CMS experiment showing the path taken by several types of particles [17].

from to be identified. The next layer is the electromagnetic calorimeter (ECAL) where electrons and photons deposit energy through electromagnetic showers. This is followed by the hadron calorimeter (HCAL) where hadronic showers deposit most of their energy. After the calorimetry systems is the superconducting magnet which is not instrumented. Outside the magnet are the muon detection systems, which are interspersed with iron plates which form the return yoke for the magnet. Due to their high mass compared to electrons, muons do not deposit much energy in the detector and often are not stopped, so the muon system is primarily a tracking detector.

The origin of the co-ordinate system used by CMS is at the nominal interaction point. It is a right handed cartesian system with the x axis pointing towards the centre of the LHC ring and the y-axis vertically upwards, the z axis then points along the beam line. The azimuthal angle  $\phi$  and the polar angle  $\theta$  are measured from the x and z axes respectively. It is common to describe the direction of outgoing particles using  $\phi$  and their pseudo-rapidity,  $\eta$  which is defined as:

$$\eta = -\ln[\tan(\theta/2)]. \quad (2.3)$$

Distances in the  $\eta - \phi$  plane are given by  $\Delta R = \sqrt{\Delta\phi^2 + \Delta\eta^2}$ . Two other quantities often used at hadron colliders are the projections of a particle's momentum and energy in the transverse plane, these are denoted  $p_T$  and  $E_T$  respectively. The missing transverse

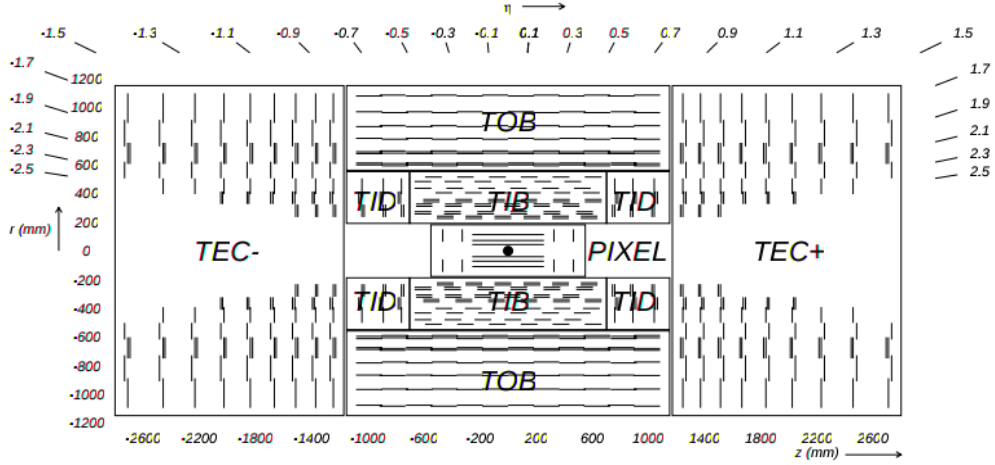


**Figure 2.7:** A cross-section of the CMS tracker, indicating the subsystems that comprise it. Each line indicates a detector module [7].

energy, defined as the negative vector sum of the momentum of all particles in an event, is important in inferring the presence of invisible particles and is denoted  $E_T^{\text{miss}}$

### 2.2.1 Tracker

The tracker is designed to precisely measure the paths of charged particles from LHC collisions which curve in CMS's magnetic field [7]. The design transverse momentum resolution of the full tracker detector is 1-2% at 100GeV. In order to precisely measure the particles' positions and ensure the occupancy of the tracker is low a high granularity is required. Due to the frequency of collisions at the LHC and the high instantaneous luminosity a radiation hard system with fast response is also necessary. This combination of requirements motivates the use of a silicon based system. When traversing silicon charged particles create electron-hole pairs, which are then separated by an applied electric field, causing a current pulse.

The tracker layout can be seen in Figure 2.7. In order to keep the sensor occupancy below 1% at design luminosity, the innermost component is a silicon pixel detector. This detector has three layers in the barrel, at radii of 4.7, 7.3 and 10.2 cm, and two in the endcap. Each pixel is 100 $\mu\text{m}$  x 150 $\mu\text{m}$  in size and in total there are 66 million of them. The resulting resolution of the pixel detector is approximately 10 $\mu\text{m}$  in the  $r - \phi$  plane and 17 $\mu\text{m}$  in the  $r - z$  plane [18].

Surrounding the pixel detector is a silicon strip detector with 10 layers in the barrel, at radii of 20 to 116 cm, and 12 pairs of disks in the endcap. The strips are typically 10-20 cm long and 80-180 $\mu\text{m}$  wide, with the strip size increasing with radius as the particle flux decreases. The strip detector's single point resolution is 230-530 $\mu\text{m}$  in the  $r - z$  plane and 23-52 $\mu\text{m}$  in the  $r - \phi$  plane. The higher resolution in the  $r - \phi$  plane allows a better measurement of  $p_T$ , as this is the direction in which the particle's tracks bend in the CMS magnetic field. The barrel and endcap detectors together have an acceptance of  $|\eta| < 2.5$  for both the pixel and strip detectors.

### 2.2.2 Electromagnetic calorimeter

The ECAL is designed to provide accurate photon and electron reconstruction and precise measurement of the electromagnetic component of hadron jets [7]. It is a homogeneous calorimeter made of lead tungstate ( $\text{PbWO}_4$ ) crystals, separated into a barrel (ECAL barrel (EB)) section, with 61200 crystals and two endcaps (ECAL endcap (EE)) each with 7234 crystals. These crystals are 25.8 radiation lengths in depth and instrumented with photodetectors, avalanche photodiodes being used in the barrel and vacuum phototriodes in the endcap.

The layout of the ECAL is shown in Figure 2.8. The EB crystals have a 170x360 arrangement in  $\eta - \phi$  space such that the gaps between crystals are offset by 3° from the vector to the detector origin, thus avoiding particles travelling through the gaps. The EB extends to  $|\eta| = 1.479$ , with higher values of  $\eta$  covered by the EE. The crystals in the EE are arranged in an  $x - y$  grid pointing at a focus 1.3m from the nominal interaction point, giving a 2 – 8° separation between the gaps between crystals and the vector to the detector origin. In addition to the main  $\text{PbWO}_4$  detector the endcaps also have a preshower detector. This preshower is a lead silicon strip sampling calorimeter, which initiates the electromagnetic showers and provides sufficient position resolution to distinguish single photons from pairs produced in neutral pion decays. The total acceptance of the barrel and endcap detectors is  $|\eta| < 3.0$ .

On entering the ECAL high energy electrons or photons initiate an electromagnetic shower by undergoing Bremsstrahlung or pair production respectively. The resulting cascade of particles continues to lose energy by successive Bremsstrahlung and pair production until their energy is low enough that the photons no longer undergo pair-production and the electrons lose their energy mainly by ionisation. The ionisation of the

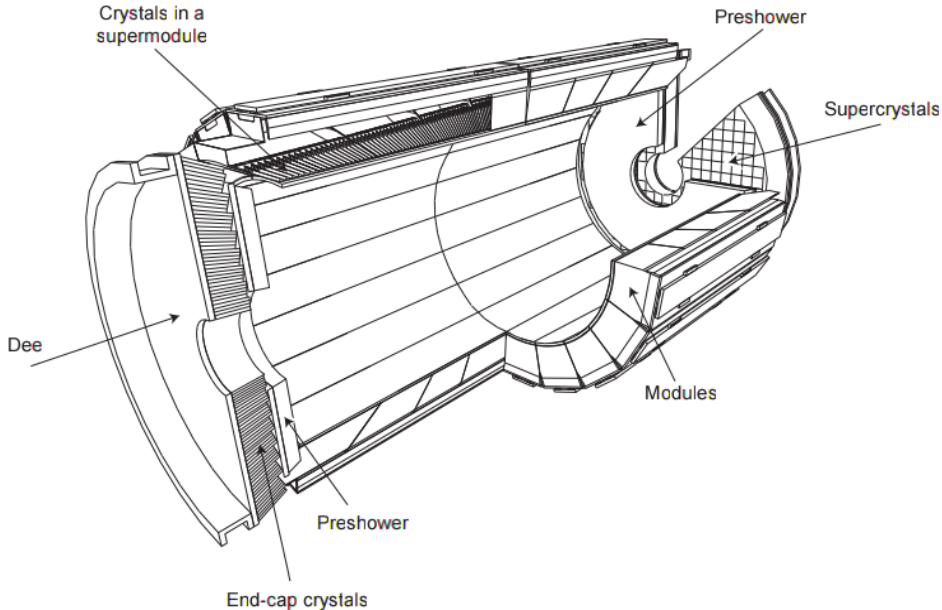


**Figure 2.8:** A schematic of the CMS ECAL, indicating the subsystems that comprise it [7].

PbWO<sub>4</sub> crystals leads to the emission of scintillation light, proportional to the amount of energy deposited, which is collected by the photodetectors.

The choice of PbWO<sub>4</sub> is motivated by its high density (8.28 g/cm<sup>3</sup>), short radiation length (0.89 cm) and small Moliére radius (2.2cm), this leads to the showers being contained in a small area and allows the calorimeter to be compact and have fine granularity. Another advantage of PbWO<sub>4</sub> is that 80% of the scintillation light is emitted within the LHC's 25ns design bunch crossing time, so particles can be properly associated with the bunch crossing they originate from.

For particle energies below 500 GeV, where the resulting shower ceases to be contained in the full depth of the ECAL, the ECAL resolution can be parametrised as:

$$\left(\frac{\sigma}{E}\right)^2 = \left(\frac{S}{\sqrt{E}}\right)^2 + \left(\frac{N}{E}\right)^2 + C^2. \quad (2.4)$$

Where  $S$  is the stochastic term,  $N$  the noise term and  $C$  the constant term. The stochastic term is comprised of fluctuations in the lateral containment of showers and also in the amount of scintillation light. The noise term is made up of electronic and digital noise, and signals from other bunch crossings which do not fully dissipate in time. The constant term comes from non-uniformity of light collection along the crystals, errors in the calibration of crystals against each other and leakage of energy from the back of

the calorimeter. The energy resolution was measured without an applied magnetic field in an electron beam using particles with momenta between 20 and 250 GeV. The stochastic, noise and constant terms were found to be  $0.028 \text{ GeV}^{1/2}$ ,  $0.12 \text{ GeV}$  and  $0.003$  respectively.

### 2.2.3 Hadronic calorimeter

The HCAL is designed to measure the energy of strongly interacting particles [7]. This measurement is particularly important for neutral hadrons which do not leave tracks in the tracking system and deposit most of their energy in the HCAL, and for the determination of  $E_T^{\text{miss}}$ . The main part of the HCAL consists of a brass and scintillator plus wavelength shifting fibre sampling calorimeter split into barrel (hadron barrel (HB)) and endcap (hadron endcaps (HE)) sections. The primary design consideration for the HCAL is that it must fit between the outer edge of the ECAL ( $r = 1.77 \text{ m}$ ) and the inner edge of the magnet ( $r = 2.95 \text{ m}$ ). In order to satisfy this requirement and achieve satisfactory containment of hadronic showers the magnet coil is also used as an absorber, and there is a further layer of scintillator outside the magnet coil (hadron outer (HO)). The barrel and endcap detectors extend to  $|\eta| < 3$ .

Brass is chosen as the main HCAL absorber because it is not magnetic and has a relatively short nuclear interaction length of 16.42 cm. Once showers have been initiated in the absorber layers they then pass through the plastic scintillator tiles, where they create pulses of light. These pulses are transferred via wavelength shifting fibres to hybrid photodiodes. The segmentation of the scintillator is such that the  $\eta - \phi$  resolution in the HB (HE) is  $0.087 \times 0.087$  (between  $0.087 \times 0.087$  and  $0.17 \times 0.17$  depending on  $\eta$ ).

In addition to the barrel and encap sections of the HCAL there is also a steel and quartz fibre Cherenkov forward calorimeter (hadron forward (HF)), which extends the calorimetry coverage of CMS to  $|\eta| < 5.2$ . The choice of this technology is driven by its ability to withstand the very high particle fluxes present so close to the beamline. Showers are initiated by the steel absorber and signals are generated in the quartz fibres by particles above the Cherenkov threshold generating Cherenkov light, which is collected by photomultiplier tubes. Due to the Cherenkov energy threshold increasing with particle mass the HF is primarily sensitive to the electromagnetic component of showers.

A diagram of the HCAL layout can be seen in Figure 2.9. In total the HCAL corresponds to 10-15 interaction lengths, depending on  $\eta$ . The resolution of the barrel and endcap sections of the HCAL as a function of the incident particle energy was measured in a

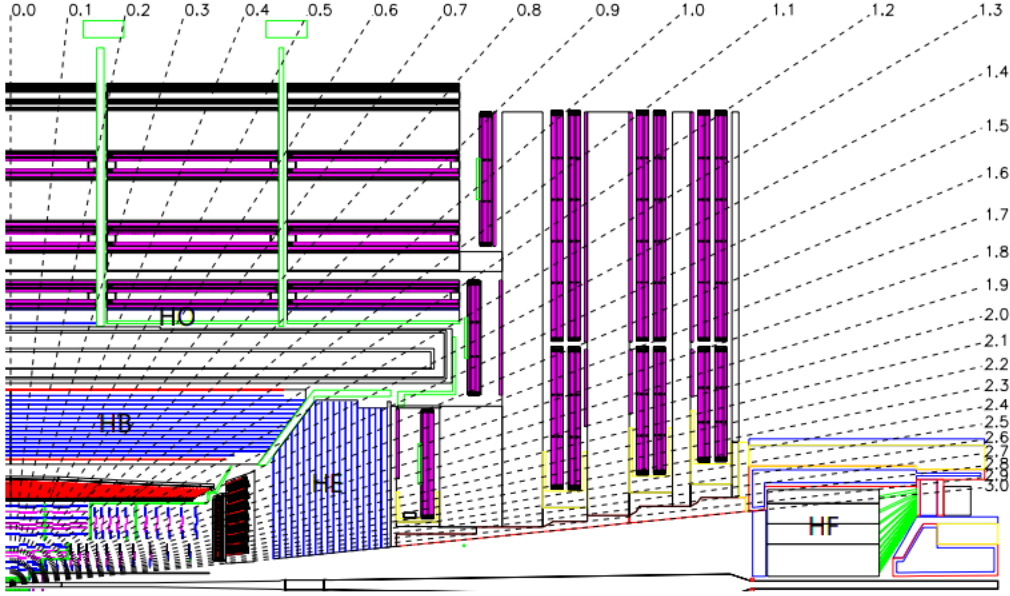


**Figure 2.9:** A schematic of a quadrant of the CMS HCAL in the  $r - z$  plane, indicating the subsystems that comprise it [7].

pion beam and has been found to be well parametrised by:

$$\left(\frac{\sigma}{E}\right)^2 = \left(\frac{94.3\%}{\sqrt{E}}\right)^2 + (8.4\%)^2 \quad [19]. \quad (2.5)$$

## 2.2.4 Muon system

As described above Muons are highly penetrating, and thus are only rarely contained by the inner detector. Very few other charged particles are able to leave the calorimeters, so the presence of tracks in the muon system is sufficient to identify muons. The muon tracking system uses three types of gaseous particle detectors, located throughout the iron magnet return yoke [7]. In all three types of detector when a charged particle travels through the gaseous detector it ionises the gas, the resulting free electrons then drift towards the detector's anode resulting in an electrical signal. The two primary types of detectors used are the drift tube (DT), which is used in the barrel section of the detector ( $|\eta| < 1.2$ ), and the cathode strip chamber (CSC), which is used in the endcap ( $0.9 < |\eta| < 2.4$ ). The DT and CSC systems identify muons and provide measurements of their momentum. These measurements can be combined with those from the tracker to improve the muon momentum resolution. This combined reconstruction and

momentum measurement is described in Section 3.5. Additionally there is a resistive plate chamber (RPC) system in both the barrel and endcap regions ( $|\eta| < 1.6$ ), the primary purpose of which is to provide trigger and bunch crossing identification information. A diagram of the CMS muons system can be found in Figure 2.10.

Each system has its own particular advantages and disadvantages which make it best suited for use in the various parts of the muon system. DTs are inexpensive and reliable, but they are not usable in regions with high muon and neutron background rates, making them well suited to the barrel portion of the detector, where large areas must be instrumented and rates are low. Each DT is a 2.4m long wire in a  $13 \times 42\text{mm}^2$  tube. The length is limited by the segmentation of the iron return yoke, and the cross-section by the requirement that the occupancy and drift time are low enough to prevent multiple muon hits being read out at the same time. The DTs are organised in 4 stations, interspersed with return yoke iron plates. The first three stations have 8 chambers each, 4 to measure the muon's position in the  $r - \phi$  plane and 4 to measure the  $z$  co-ordinate. The final outermost layer does not have the  $z$ -measuring chambers. These chambers consist of 8-12 stacked DTs, with each layer offset from the previous one by half the width of a tube to avoid gaps.

Due to their fast response time, fine segmentation and radiation resistance CSCs ideal for the endcap region where the muon and background rates are higher. Each CSC is a multiwire proportional chamber with 7 planes of cathode strips running radially outwards with 6 planes of anode wires, which run azimuthally, interleaved between them. Both the anode and cathode wires are read out to provide  $\eta$  and  $r - \phi$  co-ordinate measurements respectively. Similarly to the DT system there are 4 CSC stations in each endcap interspersed with iron return yoke plates. The position resolution in the  $r - \phi$  plane of the CSCs varies from 75-80 $\mu\text{m}$ .

The RPCs are gas gaps surrounded by anode and cathode plates with read out strips between them. The advantage of RPCs is that their response is good at high rates, and they have very good time resolution, making them ideal for use in the trigger and assignment of muons to a bunch crossing. However, they have much poorer position resolution than the DTs or CSCs. There are 6 layers of RPCs in the barrel and 3 in the endcap.

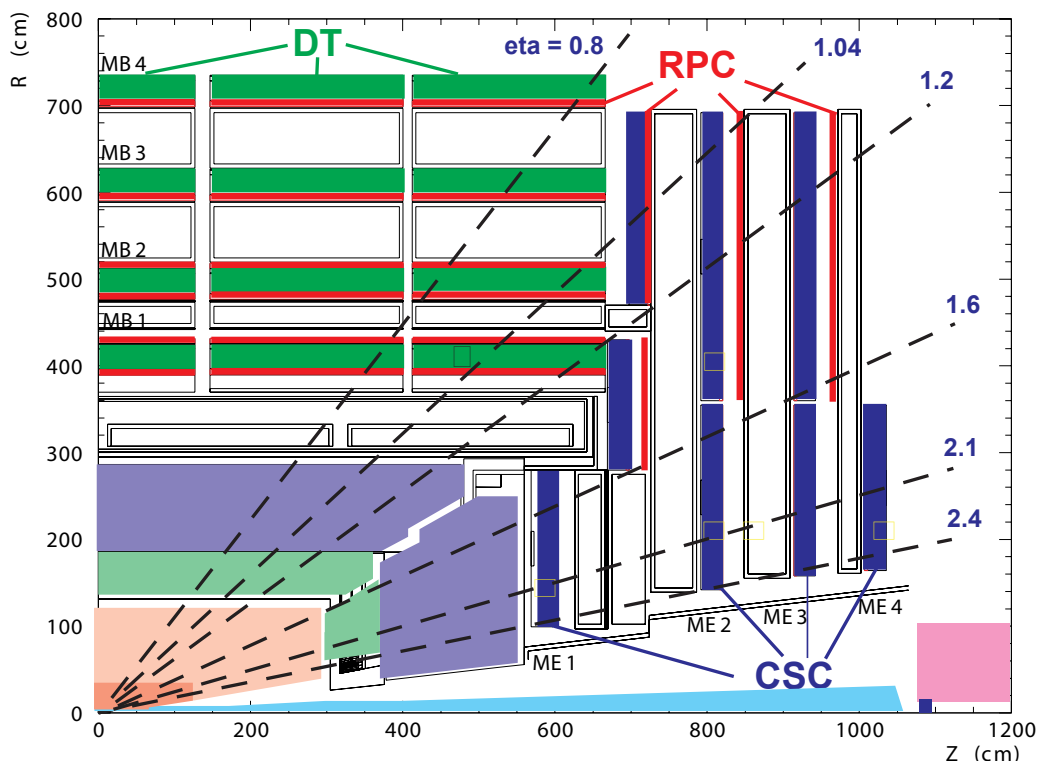


**Figure 2.10:** A schematic of a quadrant of the CMS muon system in the  $r - z$  plane, indicating the subsystems that comprise it [20].

### 2.2.5 Trigger system and data processing

The design bunch crossing rate of the LHC is 40 MHz, and for the data used in this thesis it varied from 20-40 MHz. Since each event consists of approximately 1 MB of data, writing every event to tape would correspond to a data rate of 20-40 TB/s which is not feasible. It is also not feasible for the detector electronics to read out the detector at this frequency. It is therefore necessary to use a trigger system to reduce the event rate and select only the most interesting events.

The trigger is separated into two stages, the Level-1 (L1) trigger and the high-level trigger (HLT) [7]. First the L1 trigger, which is built of custom-designed electronics, reduces the rate to a maximum of 100 kHz. The decision to accept an event in the L1 trigger or not starts with local information on the energy deposits in the calorimeters and hits in the muon systems, which is stored for all events for 128 bunch crossings. A decision must therefore be made within 128 bunch crossings or the event is discarded. Due to the limited time available and data acquisition system bandwidth available, this information is generally not available at the detector's full resolution. After it is collected from the detector the local information is then passed to the regional trigger systems, which generate lists of trigger candidates, such as electrons or jets, ranked by energy and quality. These ranked lists from each region are then passed to the global muon and calorimeter system triggers, which select the highest ranked candidates across the whole detector and give them to the global trigger, which makes a final decision. This process is shown in Figure 2.11.

If an event is accepted by the L1 trigger the full detector information is read out to the HLT farm on the surface, which reduces the rate further still to approximately 1 kHz. The HLT consists of several thousand commercially available CPUs. Despite having the full detector information, the time available does not allow for the full offline reconstruction to be performed. Never the less, the algorithms available at the HLT are much closer to those used offline than those available at L1, reducing the numbers of events lost due to differences in trigger level and offline quantities.

If they are accepted by the HLT, events are sent to be reconstructed using the Worldwide LHC Computing Grid (WLCG). The WLCG consists of several tiers. Data is first fully reconstructed at the Tier 0 centres. During Run I there was only one of these at CERN, for Run II there will also be a Tier 0 centre in Budapest. It is then sent to at least one Tier 1 centre, so that a full copy of the data is available at multiple sites in different

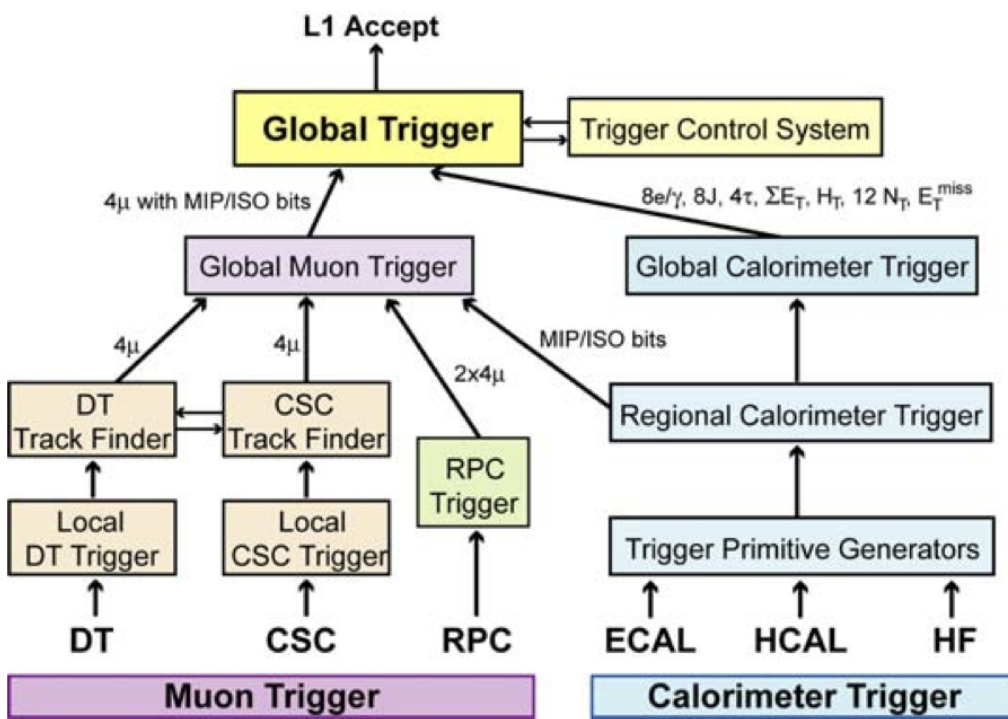


**Figure 2.11:** A schematic of the L1 trigger system. The arrows indicate the flow of data, the information transferred between systems is also indicated [7].

geographic locations. Tier 2 and 3 centres then process this data according to the needs of specific analyses.

During 2012 running it was found that it was possible for data to be written to tape from the CMS detector at a higher rate than it could be reconstructed by the Tier 0. 30% of the output of CMS was therefore immediately sent for “prompt” reconstruction, while the remainder was “parked” to tape to be reconstructed during LHC shutdown periods when there is spare computing capacity available [21]. The extra events that could be stored through this parking allowed significantly lower trigger selection thresholds to be used for some of the analyses described in this thesis.

# Chapter 3

## Physics objects and event reconstruction

**3.1 Primary vertex**

**3.2 Jets**

**3.3 Missing transverse energy**

**3.4 Electrons**

**3.5 Muons**

**3.6 Taus**

**3.7 Photons**

# Chapter 4

## Methods for limit setting

# Chapter 5

## Search for invisibly decaying Higgs bosons in run I prompt data

### 5.1 Trigger and event selection

### 5.2 Background estimation

#### 5.2.1 $W \rightarrow e\nu + \text{jets}$

#### 5.2.2 $W \rightarrow \mu\nu + \text{jets}$

#### 5.2.3 $W \rightarrow \tau\nu + \text{jets}$

#### 5.2.4 $Z \rightarrow \nu\nu + \text{jets}$

#### 5.2.5 QCD

#### 5.2.6 Minor backgrounds

### 5.3 Systematic uncertainties

### 5.4 Results



# Chapter 6

## Search for invisibly decaying Higgs bosons in run I parked data

### 6.1 Trigger

### 6.2 Event selection

### 6.3 Background estimation

#### 6.3.1 $W \rightarrow e\nu + \text{jets}$

#### 6.3.2 $W \rightarrow \mu\nu + \text{jets}$

#### 6.3.3 $W \rightarrow \tau\nu + \text{jets}$

#### 6.3.4 $Z \rightarrow \nu\nu + \text{jets}$

#### 6.3.5 QCD

#### 6.3.6 Minor backgrounds

### 6.4 Systematic uncertainties

### 6.5 Results

# **Chapter 7**

## **Combinations and interpretations of run I searches for invisibly decaying Higgs bosons**

**7.1 Searches in other channels**

**7.2 Combination with prompt VBF search**

**7.3 Combination with the parked VBF search**

**7.4 Dark matter interpretations**

# Chapter 8

## Search for invisibly decaying Higgs bosons in run II data



# Bibliography

- [1] D. Hanneke, S. Fogwell, and G. Gabrielse, “New Measurement of the Electron Magnetic Moment and the Fine Structure Constant”, *Phys. Rev. Lett.* **100** (Mar, 2008) 120801, [doi:10.1103/PhysRevLett.100.120801](https://doi.org/10.1103/PhysRevLett.100.120801).
- [2] E. Noether, “Invariant Variation Problems”, *Gott. Nachr.* **1918** (1918) 235–257, [doi:10.1080/00411457108231446](https://doi.org/10.1080/00411457108231446), [arXiv:physics/0503066](https://arxiv.org/abs/physics/0503066). [Transp. Theory Statist. Phys.1,186(1971)].
- [3] E. Noether, “Invariant variation problems”, *Transport Theory and Statistical Physics* **1** (1971), no. 3, 186–207, [doi:10.1080/00411457108231446](https://doi.org/10.1080/00411457108231446).
- [4] C. N. Yang and R. L. Mills, “Conservation of Isotopic Spin and Isotopic Gauge Invariance”, *Phys. Rev.* **96** (Oct, 1954) 191–195, [doi:10.1103/PhysRev.96.191](https://doi.org/10.1103/PhysRev.96.191).
- [5] Particle Data Group Collaboration, “Review of Particle Physics”, *Chin. Phys. C* **38** (2014) 090001, [doi:10.1088/1674-1137/38/9/090001](https://doi.org/10.1088/1674-1137/38/9/090001).
- [6] D. Griffiths, “Introduction to Elementary Particles”. Physics textbook. Wiley, 2008.
- [7] C. Collaboration, “The CMS experiment at the CERN LHC”, *JINST* **3** (2008) S08004, [doi:10.1088/1748-0221/3/08/S08004](https://doi.org/10.1088/1748-0221/3/08/S08004).
- [8] L. Evans and P. Bryant, “LHC Machine”, *JINST* **3** (2008), no. 08, S08001, [doi:10.1088/1748-0221/3/08/S08001](https://doi.org/10.1088/1748-0221/3/08/S08001).
- [9] LEP Injector Study Group, “LEP design report, volume I: The LEP injector chain; LEP design report, volume II: The LEP Main Ring”. CERN, Geneva, 1983.
- [10] A. Collaboration, “The ALICE experiment at the CERN LHC”, *JINST* **3** (2008) S08002, [doi:10.1088/1748-0221/3/08/S08002](https://doi.org/10.1088/1748-0221/3/08/S08002).
- [11] A. Collaboration, “The ATLAS Experiment at the CERN Large Hadron Collider”, *JINST* **3** (2008) S08003, [doi:10.1088/1748-0221/3/08/S08003](https://doi.org/10.1088/1748-0221/3/08/S08003).

- [12] LHCb Collaboration, “The LHCb Detector at the LHC”, *JINST* **3** (2008) S08005, [doi:10.1088/1748-0221/3/08/S08005](https://doi.org/10.1088/1748-0221/3/08/S08005).
- [13] M. Benedikt, P. Collier, V. Mertens et al., “LHC Design Report”. CERN, Geneva, 2004.
- [14] CMS Collaboration, “CMS Luminosity - Public Results”, .
- [15] W. J. Stirling, “Private communication”, .
- [16] T. Sakuma and T. McCauley, “Detector and Event Visualization with SketchUp at the CMS Experiment”, *J. Phys.: Conf. Ser.* **513** 022032, [doi:10.1088/1742-6596/513/2/022032](https://doi.org/10.1088/1742-6596/513/2/022032).
- [17] CMS Collaboration, “Interactive Slice of the CMS detector”, *CMS Document 4172-v2*.
- [18] Tricomi, Alessia, “Performances of the ATLAS and CMS silicon tracker”, *Eur Phys J C* **33** (2004) s1023–s1025, [doi:10.1140/epjcd/s2004-03-1801-1](https://doi.org/10.1140/epjcd/s2004-03-1801-1).
- [19] USCMS, ECAL/HCAL Collaboration, “The CMS barrel calorimeter response to particle beams from 2-GeV/c to 350-GeV/c”, *Eur. Phys. J.* **C60** (2009) 359–373, [doi:10.1140/epjc/s10052-009-0959-5](https://doi.org/10.1140/epjc/s10052-009-0959-5), [10.1140/epjc/s10052-009-1024-0](https://doi.org/10.1140/epjc/s10052-009-1024-0). [Erratum: Eur. Phys. J.C61,353(2009)].
- [20] CMS Collaboration Collaboration, “CMS Physics: Technical Design Report Volume 1: Detector Performance and Software”. Technical Design Report CMS. CERN, Geneva, 2006. There is an error on cover due to a technical problem for some items.
- [21] CMS Collaboration Collaboration, “Data Parking and Data Scouting at the CMS Experiment”, .

# List of Figures

2.1	The layout of the LHC accelerator chain, showing the position of the four main detectors. . . . .	11
2.2	A summary of the luminosity delivered to CMS during Run 1 of the LHC[14].	13
2.3	Cross sections for several processes in collisions of protons with protons or anti-protons as a function of centre of mass energy. The energies that the LHC and Tevatron ran at are highlighted[15]. . . . .	14
2.4	Distribution of the number of interactions per bunch crossing in CMS during 2012 running of the LHC[14]. . . . .	15
2.5	A diagram of the subsystems making up the CMS detector, illustrating the hermeticity and layered structure of the experiment[16]. . . . .	16
2.6	A schematic cross-section of the CMS experiment showing the path taken by several types of particles[17]. . . . .	17
2.7	A cross-section of the CMS tracker, indicating the subsystems that comprise it. Each line indicates a detector module[7]. . . . .	18
2.8	A schematic of the CMS ECAL, indicating the subsystems that comprise it[7]. . . . .	20
2.9	A schematic of a quadrant of the CMS HCAL in the $r - z$ plane, indicating the subsystems that comprise it[7]. . . . .	22
2.10	A schematic of a quadrant of the CMS muon system in the $r - z$ plane, indicating the subsystems that comprise it[20]. . . . .	24
2.11	A schematic of the L1 trigger system. The arrows indicate the flow of data, the information transferred between systems is also indicated[7]. . .	26

# List of Tables

1.1	The fundamental fermions observed in nature separated into their three generations. Each particle shown also has an antiparticle with opposite charge and identical mass. Values taken from[5] . . . . .	3
1.2	The fundamental vector bosons observed in nature separated by the force which they mediate. Values taken from[5]. . . . .	4

# List of Acronyms

**PSB** Proton Synchrotron Booster

**PS** Proton Synchrotron

**SPS** Super Proton Synchrotron

**PU** pile-up

**SM** standard model

**BSM** beyond the SM

**QFT** quantum field theory

**ECAL** electromagnetic calorimeter

**HCAL** hadron calorimeter

**EB** ECAL barrel

**EE** ECAL endcap

**HB** hadron barrel

**HE** hadron endcaps

**HF** hadron forward

**HO** hadron outer

**L1** Level-1

**HLT** high-level trigger

**CSC** cathode strip chamber

**DT** drift tube

**RPC** resistive plate chamber

**WLCG** Worldwide LHC Computing Grid